Morphogenesis in metal electrodeposition

Benedetto Bozzini

Dipartimento di Ingegneria dell'Innovazione, Università del Salento
Via per Monteroni, 73100 Lecce, Italy
Tel.: +39-0832-297323, `benedetto.bozzini@unisalento.it`

Deborah Lacitignola

Dipartimento di Scienze Motorie e della Salute, Università di Cassino,
Campus Folcara, Loc. S.Angelo, I-03043 Cassino, Italy
`d.lacitignola@unicas.it`

Claudio Mele

Dipartimento di Ingegneria dell'Innovazione, Università del Salento,
Via per Monteroni, 73100 Lecce, Italy
`claudio.mele@unisalento.it`

Ivonne Sgura

Dipartimento di Matematica e Fisica "E. De Giorgi", Università del Salento,
Via per Arnesano, 73100 Lecce, Italy,
`ivonne.sgura@unisalento.it`

Abstract. This paper offers an overview of morphogenetic processes going on in metal electrodeposition processes and provides a systematisation of the morphology classes identified experimentally in terms of an electrokinetic theory accounting for charge-transfer and mass-transport rates. In addition, it provides a review of the modelling work by the authors, based on a reaction-diffusion system coupling morphology with surface chemistry of the growing metal and briefly describes the experimental validation of the model.

1 Introduction

Metal plating is a well-assessed and widespread technology, ubiquitous in surface treatment technologies, economically interesting owing to low investment and managing costs in comparison with competing coating techniques and exhibiting a wide-range of applications including, among others: energetics (fuel cells and batteries), chemical and biochemical sensors, electronic fabrication, corrosion and wear protection, surface nobilitation and decoration, preservation of metallic components, ranging from heritage to nuclear and aerospace.

The successful implementation of metal plating in many cutting-edge technologies seems the only viable approach to certain material fabrication issues, especially in the nanoscale (e.g. state-of-the-art and next-generation ULSI technologies, durability of GenIV nuclear reactors, neuroelectrochemical transducers). Though being a mature process[1], the fundamental knowledge of the physicochemical bases of electrochemical metal growth and, in particular, of its dynamics, is still poorly known. The difficulties found in working out a physically insightful and predictive mathematical modelling of the complex multiscale and multiphysics problem underlying the overall electrochemical metal growth are delaying the coherent assembly of the extensive though widely scattered information available on single aspects of the process, such as crystallisation, electrochemical kinetics and mass transport. In fact, the modelling of electrodeposition (ECD) morphology has received considerable attention in the past (see references contained in [22]), nevertheless more extensive and insightful investigations are still required, in particular as far as the achievement of predictive capabilities is concerned. In fact, the ability of producing controlled metal morphologies, based on molecular properties of the growing surface and of adsorbates, would allow to make profit of the unique features of the electrochemical growth approach to high-technology areas that are limited by lithographic techniques.

As a result of the present state of affairs, the functional and aesthetic quality of metal coatings is achieved on the basis of empiricism to the best of the authors' understanding none of the available industrial processes or process improvement actions have been developed with a knowledge-based approach, but rather by trial-and-error or through analogy arguments. Moreover, a curious outcome of the empirical approach to morphology control is that, in most cases, industrial success of this class of processes is achieved at the cost of using extremely toxic and polluting additives. Unfortunately - notwithstanding extensive academic and industrial efforts to improve both products and process chemistries - electroplating can be regarded as one of the most polluting industries. In fact, apart from the plating of intrinsically environmentally unfriendly metals - made necessary by their unique functional properties (hardness, wear resistance, optical properties, corrosion resistance), such as: cadmium, chromium and nickel - essentially all industrially viable processes for the ECD of non-toxic metals, e.g.: silver, gold and zinc, contain evocative poisonous additives, e.g.: arsenic (for bright gold), strychnine (for nickel free of pinholes) and cyanide (for gold,

---

[1]Silver plating is in fact the first known application of Volta's battery in 1801; aluminum electrolysis was used to fabricate Napoleon III's tableware for very special occasions at the imperial French court, present-day decorative- and hard chromium electrodeposition thrive on a patent dating back to 1860. Furthermore, a recent publication has proved one application of multilayer metal electrodeposition dating back to the II century b.C. [25]

silver, copper, zinc and cadmium).

In this paper we discuss, from both the experimental and the mathematical points of view, the peculiarities of metal growth by ECD. We shall: (i) highlight the key phenomenological points of metal growth morphology and systematise them in terms of simple rate equations as well as (ii) propose a tentative rationalisation in terms a system of coupled reaction-diffusion describing morphogenesis at the electrochemical interface during metal plating at controlled potential. The presented material will be based on a series of recent papers [16, 18, 19, 23, 24] in which we have pinpointed the fact that some peculiarities of the coupling of morphological and surface chemical dynamics - modelled in terms of a system of reaction-diffusion equations - allows to gain control over the 3D electrocrystallisation process, giving rise to pattern formation as well as the development of transition front waves in the morphology and surface chemistry, with travelling waves, moving with specific wave speed. Furthermore, we have shown that such dynamics exhibits some subtle interactions with an applied forcing frequency, giving rise to intriguing effects that are likely to have a bearing on the development of green metal plating chemistries.

2   Generalities on electrodeposition processes

Metal ECD is a cathodic electrochemical process in which metal cations, present in an electrolyte solution in contact with the cathode to be covered with metal - in order either to achieve a coating or to form a freestanding object -, are reduced to the metal M according to the following reaction scheme:

$$M^{z+} + z\,e^- \ \rightarrow M, \tag{1}$$

where M^{z+} represents the cation, e^- denotes the electron, z is the valency. This reduction is obtained by circulating electric current through a system composed of the cathode, electrolyte, anode (supporting electrode in order to ensure electrical continuity) and an external circuit incorporating a generator. The system is schematically depicted in Fig.1.

The addition of atoms to the solid cathode via the reaction of Eq.(1) gives rise to the development of growth morphologies that have a tremendous impact on the functional properties of the coatings. A selection of representative examples is reported below.
(i) Continuity determines properties such as corrosion protection (e.g. corrosion resistant films) and magnetic properties (e.g. soft magnetic computer read-write heads).
(ii) Smoothness controls: wear resistance (e.g. tribological coatings), electrical
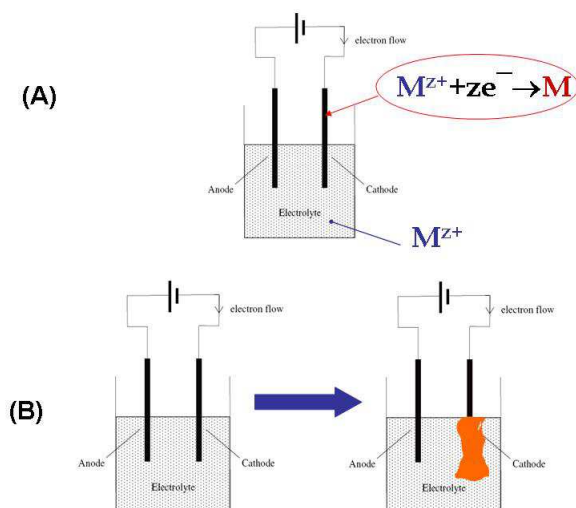
Figure 1. Electrical and chemical scheme of an electrodeposition process. (A) Electrical circuit of an electrochemical cell, with indication of the cathodic metal reduction process; (B) accretion of metal at the cathode as a result of the electroreduction reaction.

performance (e.g. Cu interconnects in semiconductor fabrication), magnetisation performance (e.g. hard magnetic layer of computer hard-disks).
(iii) Porosity is a key quantity for the ECD catalytic materials (e.g. fuel cell electrodes and electrocatalytic electrodes).
(iv) Furthermore, ECD is a pathway to the growth of nanostructures: a tremendous range of objects displaying dimension-dependent physics has been formed by ECD, such as nanoparticles, nanowalls, nanotubes. The use of template-directed ECD also offers the possibility of fabricating arrays of nanostructures connected in parallel.

From the above-listed examples, the overwhelming importance of morphology control can be easily grasped. Unfortunately, morphology control is an entangled multiscale problem exhibiting technologically important scales ranging from that of the object (cm-mm) to the atomic dimensions (Å) (surface diffusion and incorporation of freshly electroreduced atoms, for details see Section 3.1, where "adatoms" are introduced and discussed), with several important processes going on also at the nano- to micro scale - such as crystallite formation and step dynamics - and at the mesoscale (several μ m) - such as mass-transport and current density distribution.
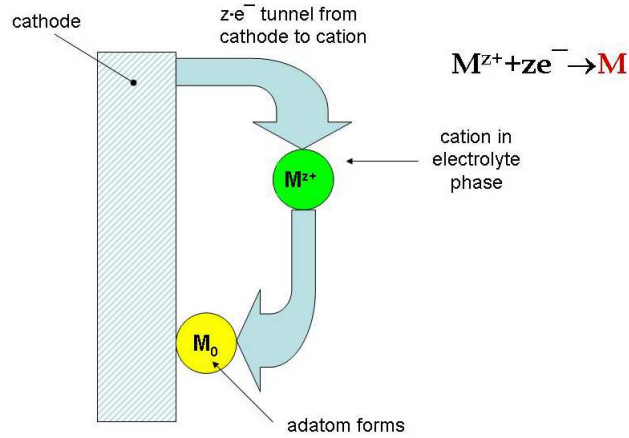
Figure 2. Pictorial description of the cathodic electroreduction process of a cation M^{z+} leading to the formation of an adatom M^0.

3   Overview of the physics of morphogenesis in electrodeposition

In the present Section we shall offer a simplified qualitative description of the essential physical underlying morphogenesis in ECD. A simple unified quantitative theory of morphogenesis will be delayed until Section 4 and a review of mathematical modelling in terms of reaction-diffusion systems will be presented in Section 5.

3.1   From cations to metallic adatoms

In the reference case of single-metal ECD, the prototypical electrochemical reaction - better specifying the Eq.(1) is:

$$M^{z+} + ze^- \ \leftrightarrow M_{ad}, \tag{2}$$

where M_{ad} indicates the adatom (i.e. atom adsorbed at the substrate surface).

This process can be pictorially represented as in Fig.2: z electrons tunnel from the cathode to the cation M^{z+} present in the electrolyte (the present treatment does not require a more insightful description of the relative collocation of cathode and cation) and produce a metallic atom that cannot reside in the electrolyte but adsorbs onto the cathode, receiving the denomination of "adatom". The rate equations for the process described by Eq.(2) will be discussed in Section 4.1.

Table 1. Surface crystal sites and corresponding adsorption energies for adatoms, for the case of a simple cubic crystal lattice and cubic adatoms. E_{coh} denotes the cohesion energy of a metallic atom belonging to the crystal bulk (degree of coordination: 6).

name	degree of coordination	adsorption energy
adatom	1	$E_{coh}/6$
step	2	$E_{coh}/3$
kink	3	$E_{coh}/2$
surface atom	5	$5E_{coh}/6$

3.2 Incorporation of adatoms into the surface crystal lattice

Adatoms land in random locations of the cathodic surface, that do not necessarily correspond to energy minima: they thus typically diffuse on the surface seeking a minimum in adsorption energy (Fig.3A). Of course, the fate of adatoms - in conjunction with the local rate of adatom formation - is a key factor in controlling surface morphology, as schematically described in Fig.4: as deposition rate and time increase, first metal is nucleated on the initially bare cathode surface (see Section 4.2): if nuclei can coalesce (see Section 4.2.2) they give rise to a thin and compact film that subsequently grows into a 3D deposit. Such initially planar 3D growth front, typically destabilises (see Section 4.4) giving rise to progressive more complex growth, generally disperse morphologies, such as globular roughness (see Section 4.4.1), structured globular structures (typically cauliflower-type see Section 4.4.2), projecting outgrowth features (see Section 4.4.3) with different morphologies, such as dendrites, powders and spongy metal. It is worth noting that nanostructures - in the form of freestanding (unsupported) objects or assembled into arrays (supported) - can be formed either implicitly [1, 11, 12] or deliberately [20] by making profit of the different types of growth modes both in stable and unstable conditions.

A crystal surface exhibits several types of defects, the most typical ones are depicted in Panels B and C of Fig.3. Panel C shows an experimental micrograph obtained by Scanning Tunneling Microscopy (STM) of a typical assembly of surface defects, while panel B offers a conceptual scheme of the same system. Within the conceptual framework set by Fig.3B, we can assume that an adatom is a cube and that the crystal lattice of the cathodes is simple cubic. One can identify the adsorption energy corresponding to a given site by the degree of coordination of the adatoms with the surface crystal (i.e. number of adatom faces in contact with the surface crystal). This way, surface crystal sites and corresponding energies can be classified as shown in Table 1.

Thus, incorporation is progressively more favored as the adsorption energy
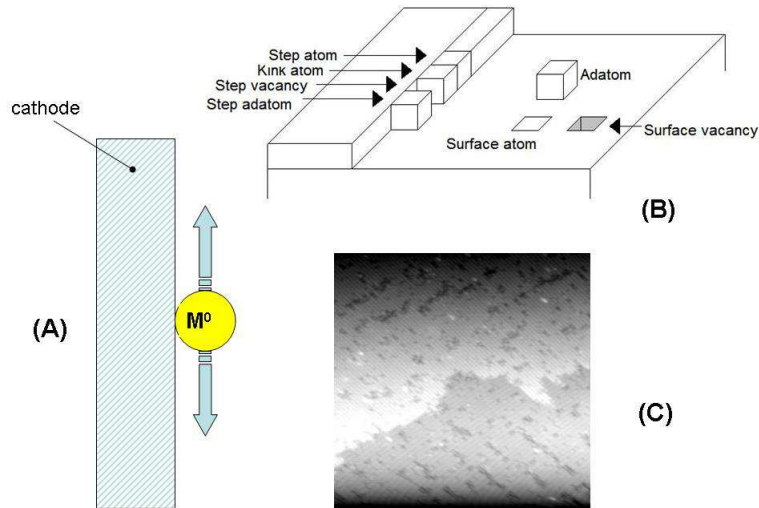
Figure 3. Diffusing adatoms and their fixation in surface crystal sites. (A) Adatoms diffuse on atomic planes of the cathode surface. (B) Simplified illustration of the crystalline surface sites. (C) Scanning Tunneling Microscopy (STM) image of a Si(100) surface, showing a complete set of surface sites (http://en.wikipedia.org/wiki/Terrace_ledge_kink)

increases: if a high energy is made available, through an external electric power source, (high-dissipation process) adatoms are relatively stable and can assemble into islands (for quantitative details, see Section 4.2), otherwise (low-dissipation process) diffusing adatoms typically become incorporated into kinks or steps. A pictorial description of these facts is offered in Fig.5. Encounters between adatoms and among small adatom clusters and further adatoms give rise to islands whose energy content is a function of the dimension and shape of the cluster itself: in particular - under given electrochemical conditions - a critical dimension exists below which the cluster is unstable and tends to redissolve into loose, diffusing adatoms. It is worth noting that, once formed, islands are confined by a step where adatoms can be fixed with a lower-energy process.

3.3   Incorporation of adatoms into steps and growth by step flow

According to Panel 1 of Fig.5, discussed in the previous Section, the low-dissipation process for the incorporation of fresh atoms into the crystal lattice of the growing electrodeposit, leads to the growth of steps over flat terraces: for obvious reasons, this process is often denominated "step flow". Of course,
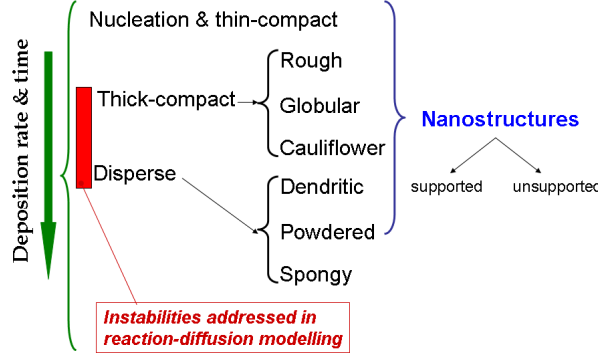
Figure 4. Scheme of the types of morphologies developing in ECD as a function of deposition rate and time.

the rate of step flow can be readily evaluated from the total rate of adatom reduction and the step density. The latter quantity is a geometrical property that can be assessed by some form of microscopy and the former one from the model discussed in Section 3.4 below. A sequence of STM images showing an instance of step-flow process in Cu electrodeposition from an acidic sulphate solution is shown in Fig.6.

3.4 General expression of electrodeposition rate in terms of first-order Arrhenius-type kinetics (accounting for both charge-transfer and mass-transport contributions)

We define $C = [M^{z+}]$ the cation concentration and $C_{ad} = (M_{ad})$ the surface adatom concentration. The first-order rate equations for the forward and backward reactions of Eq.(2) are:

$$\overrightarrow{i} = \overrightarrow{k} \, C, \quad \overleftarrow{i} = \overleftarrow{k} \, C_{ad}, \quad i_{tot} = \overrightarrow{i} - \overleftarrow{i}, \tag{3}$$

where $\overrightarrow{i}$ and $\overleftarrow{i}$ indicate the forward (cathodic) and backward (anodic) current densities (c.d.), respectively. Their sum i_{tot} is proportional to the growth rate through Faraday's equation. In terms of sign convention: we stick to the usual one of defining cathodic c.d.s as negative: thus $\overrightarrow{i} < 0$ (cathodic reaction), $\overleftarrow{i} > 0$ (anodic reaction) and for ECD: $i_{tot} < 0$.

Denoting by V_{eq} the nernstian potential corresponding to the equilibrium of Eq.(2) and V_{appl} the potential applied to the electrode-electrolyte interface (i.e. growth interface), the overvoltage η (dissipation) is defined as:

$$\eta = V_{eq} - V_{appl}. \tag{4}$$

Figure 5. Illustration of the modes of adatom incorporation into the surface crystal lattice: (1) surface diffusion and incorporation into step, resulting in step flow; (2) formation of clusters.

The adopted sign convention for c.d.s is typically accompanied by a sign convention on potentials such that $\eta < 0$ for cathodic processes and $\eta > 0$ for anodic ones.

Interpreting the kinetic constants of Eq.(3) in terms of Arrhenius expressions and taking into account the fact that the activation energy contains an electrical contribution, expanding the electrical contribution to first order, one can write:

$$\begin{cases} \overrightarrow{k} = \overrightarrow{A} \exp\left(-\dfrac{E_{act}}{RT}\right) = \overrightarrow{A} \exp\left(-\dfrac{E_{act}^{chem}}{RT}\right) \exp\left(-\dfrac{E_{act}^{electr}}{RT}\right) \\ \qquad\qquad = \overrightarrow{k}_{chim} \exp\left(-\dfrac{\eta}{B_c}\right) \\ \overleftarrow{k} = \overleftarrow{k}_{chim} \exp\left(-\dfrac{\eta}{B_a}\right) \end{cases}$$

Where B_c and B_a are positive real constants, called cathodic and anodic Tafel slopes, respectively, R is the gas constant and T is the absolute temperature. Assuming that $\overrightarrow{k}_{chim}$ and $\overleftarrow{k}_{chim}$ are positive real constants and inserting Eq.s (3.4) into (3), we get:

$$i_{tot} = \overleftarrow{k}_{chim} C_{ad} \exp\left(\frac{\eta}{B_a}\right) - \overrightarrow{k}_{chim} C \exp\left(-\frac{\eta}{B_c}\right). \qquad (5)$$

Of course, in general, C and C_{ad} are local, instantaneous quantities and adequate mass-transport equations ought to be coupled with Eq.(5) to obtain a complete

Figure 6. Sequence of STM images illustrating step-flow during the electrodeposition of Cu from a CuSO$_4$ 1 mM, H$_2$SO$_4$ 0.5 M solution at -800 mV vs Ag/AgCl. The height of the steps is monoatomic.

description of the ECD rate. At equilibrium $i_{tot} = 0$ and $\eta = 0$, implying that:

$$\overleftarrow{k}_{chim}C_{ad,o} - \overrightarrow{k}_{chim}C_0 = 0, \tag{6}$$

where C_0 and $C_{ad,o}$ denote the equilibrium values. Whence, Eq.(5) can be rewritten as:

$$i_{tot} = i_0 \left[\frac{C_{ad}}{C_{ad,o}} \exp\left(\frac{\eta}{B_a}\right) - \frac{C}{C_o} \exp\left(-\frac{\eta}{B_c}\right) \right], \quad i_0 = \overleftarrow{k}_{chim}C_0 \tag{7}$$

It is worth noting that this notation is able to capture the electrokinetic effects of inhibiting additives. In fact, for a given i_{tot}, a higher is required in the presence of additives with respect to the additive-free case. Dually, if is fixed, lower i_{tot} values are obtained in the presence of additives. Assuming, for simplicity, that the anodic-going reaction is not affected by the presence of additives, this scenario can be described by the simple relationship: B_c(with additives) $> B_c$ (without additives).

In the following sections, inspiration is derived from the outstanding work [27] and reference is made to the terminology proposed in this book and literature quoted therein: nevertheless, a different approach is developed in three chief respects: (i) a unified - though approximated and semi-quantitative - theory is

proposed to account for the principal typologies of cathodic growth morphologies; (ii) the physico-chemical basis underlying the electrokinetic expressions has been modified in many points. This in view of a generalised and consistent description of the combination of charge-transfer and mass-transport controlled kinetics prevailing in the ECD conditions that give rise to the different types of morphology; (iii) the mathematical treatment of electrokinetics has been modified in many essential points.

3.5   Nucleation processes

If enough energy is available during the electroreduction process, for the system to follow the high-dissipation path presented in Fig.52, the metal will grow via the formation of separate nuclei on terraces, rather than by the flow of steps confining the terraces. A selection of examples - derived from [28] - is provided in Fig.7 and a simple quantitative discussion of the nucleation energy in the electrochemical context is offered in the next paragraph.

3.5.1 Nucleation overvoltage   It is possible to associate part of the dissipation to the nucleation process and thus define

$$\eta_{tot} = \eta_{ct} + \eta_{nucl} \tag{8}$$

where: η_{tot} is the total overvoltage, η_{ct} is the charge-transfer overvoltage and η_{nucl} the nucleation overvoltage - related to the formation of the critical nucleus. It should be noted that $\eta_{nucl}(i = 0) = 0$ because the adatoms that are reduced under conditions not allowing the formation of the critical nucleus consume charge, but this same charge is regained when the adatoms desorb after having diffused on terraces without stabilising into nuclei. Thus η_{nucl} can be regarded as a "delay" of the onset of a steady-state reduction current density with respect to the equilibrium nernstian potential. Thus - as an extension of Eq.(4) -, we can write:

$$\eta_{ct} = V_{eq} - V_{appl} = (V_{nerst} - \eta_{nucl}) - V_{appl} \tag{9}$$

Considering Eq.s(4) - defining the out-of-equilibrium quantity η (containing all physical contributions to the departure from equilibrium) - and (9) - defining the out-of-equilibrium quantity η_{ct} due just to the change transfer process - together, we can conclude that: (i) η_{ct} in Eq.(9) is the effective overvoltage (i.e. the fraction of the energy dissipation) that is able to impact charge; (ii) the total overvoltage η in Eq.(4) is meant as distance from the nernstian potential, thus Eq.(4) can be restated as: $\eta = V_{nerst} - V_{appl}$ pinpointing that only the nernstian potential term of the thermodynamical potential (i.e. an atomically
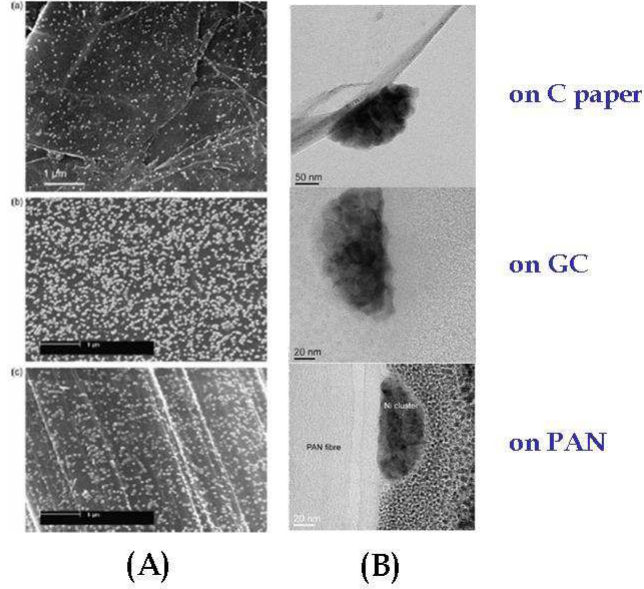
Figure 7. Examples of nucleation: Ni from chloride bath [28]. (A) SEM images show-ing the effect of the cathodic substrate material (C: graphite, GC: glassy carbon, PAN: polyaniline) on nucleation density. (B) HRTEM images of single Ni nuclei on the cor-responding substrate.

flat electrode is considered) is taken into account in defining η, and eventually (see also Eq. (8)):

$$\eta = V_{nerst} - V_{appl} = \eta_{ct} + \eta_{nucl}. \tag{10}$$

The equation states that the formal overall dissipation η can be divided into η_{ct} a charge-transfer component (i.e. strictly kinetic one) and η_{nucl} a nucleation one (that is strictly thermodynamic, but is regarded as a departure from an ideally flat geometry). The overvoltage as defined in Eq.(10) is thus the quantity that goes into the Butler-Volmer equation, with the note of caution that if $\eta = \eta_{nucl}$ than $i_{tot} = 0$ (i.e. $i_{tot} \neq 0$ is possible iif $\eta_{ct} \neq 0$). This point is expanded below and actually used to define the nucleation overvoltage η_{nucl}. Assuming that: (i) mass-transport does not affect kinetics, i.e. $C = C_0$ and (ii) $i_{tot} = 0$ (i.e. $\eta_{ct} = 0$), from Eq. (7) it results:

$$\eta_{nucl} = -\frac{B_a \, B_c}{B_a + B_c} ln \frac{C_{ad}}{C_{ad,o}}. \tag{11}$$
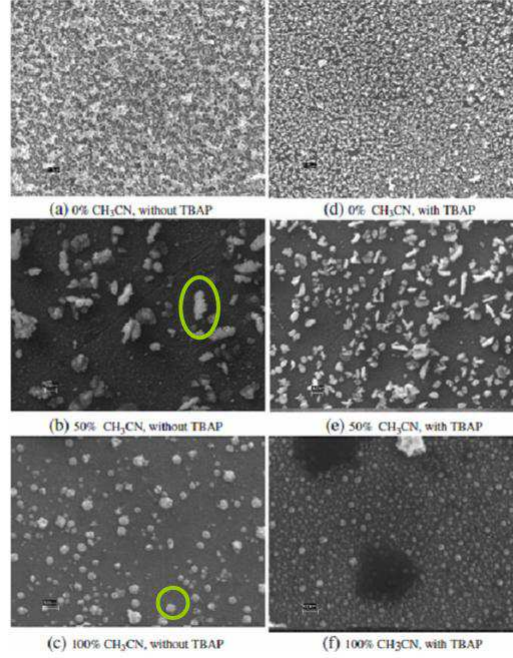
Figure 8. Examples of nucleation-exclusion zone. Electrodeposition of Ag from mixed organic-aqueous solutions, in absence and in presence of an additive [26].

In the special case - often encountered in the literature - of a symmetry charge-transfer barrier for cathodic and anodic processes: $B_a = \frac{RT}{zF\alpha}$, $B_c = \frac{RT}{zF(1-\alpha)}$, it results: $\eta_{nucl} = -\frac{RT}{zF} ln \frac{C_{ad}}{C_{ad,o}}$.

3.5.2 The nucleation-exclusion zone As one can notice from Fig.8, typically there exists an area around a formed nucleus where other nuclei do not form: this phenomenon is due to current density screening caused by pre-existing nuclei. Under the assumption of ohmically controlled overvoltages and spatially homogeneous current density i, one can associate the nucleation over-voltage η_{nucl} to a given distance between the electrode surface and a point in the electrolyte. If we wish to form a new nucleus on a planar electrode, we need to develop locally an overvoltage η such that at: $|\eta| \geq |\eta_{nucl}|$. The hypothesis of ohmic overvoltage control allows to associate h to geometry. Fig.9 shows that, for the planar part of the electrode: $\eta_{nucl}[V] = \rho\Omega cm \cdot l[cm] \cdot i[\frac{A}{cm^2}]$, where ρ is the resistivity of the electrolyte and the meaning of l is clear from Fig.9.
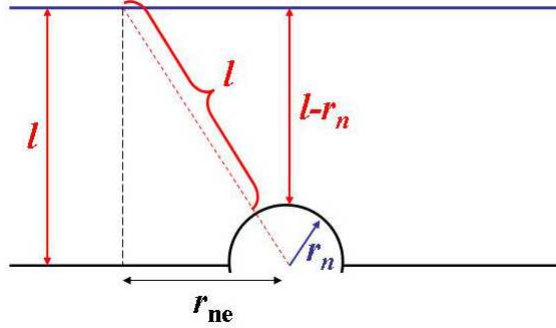
Figure 9. Scheme of the process giving rise to the formation of a nucleation-exclusion zone. Legenda - l: distance within the electrolyte, corresponding to the ohmically controlled nucleation overvoltage.

Presence of a circular (in 2D) nucleus of radius r_n gives rise to a distorsion of the current density distribution, that can be naively modelled as shown in Fig.9 and brings about the existence of a region of extension r_{ne} from the center of the nucleus - called *nucleation exclusion zone* -, where $|\eta| \leq |\eta_{nucl}$ and thus further nucleation cannot take place. By straightforward geometry it can be proved that $r_{ne} = r_n \sqrt{\frac{2l}{r_n} + 1} = r_n \sqrt{\frac{2\eta_{nucl}}{r_n \rho i} + 1}$. This simple equation is able to capture the relevant phenomenology, namely:

$$\lim_{\eta_{nucl} \to 0} r_{ne} = r_n, \quad \lim_{i \to \infty} r_{ne} = r_n, \quad \lim_{\rho \to \infty} r_{ne} = r_n,$$

$$\lim_{\eta_{nucl} \to \infty} r_{ne} = \infty, \quad \lim_{\rho \to 0} r_{ne} = \infty.$$

3.5.3 Critical nucleus   The critical nucleus is the nucleus containing the minimum number of adatoms required to ensure its stability. It can be estimated through a simple energy balance. The Gibbs free energy $\Delta G(N)$ of a nucleus containing N adatoms can be written as:

$$\Delta G(N) = \Delta G_{et}(N) + \Delta G_{surf}(N),$$

where the term $\Delta G_{et}(N)$ refers to an electron-transfer and $\Delta G_{surf}(N)$ to surface energy. $\Delta G_{et}(N)$ can be estimated as the electric work required to reduce the number of adatoms forming the cluster. After Eq.(10), one can write: $\Delta G_{et}(N) = -z\,eN\eta$, where e is the electron charge. $\Delta G_{surf}(N)$ can be estimated from simple energetic and geometric considerations as $\Delta G_{surf}(N) =$
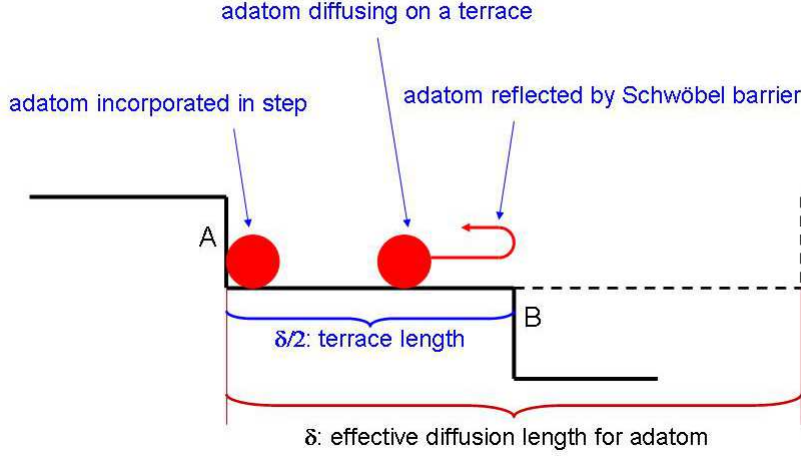
Figure 10. Schematic 1D view of the diffusion process undergone by an adatom on a terrace: the adatom is confined between the positive step A, where it becomes incorporated and the negative step B, where it is reflected by the *Schwöbel* barrier.

$E_{step} P(N)$, where E_{step} is the step energy, defined above in Section 3.2 (see also Table 1 and Fig. 3) and P is the perimeter of the nucleus. $P(N)$ can be evaluated with the following simple steps. Let us identify the area $A(N)$ of the nucleus composed of N adatoms with the area of an adatom multiplied by N, being a the adatom radius. By defining $r_{equiv} = \sqrt{N}a$ the equivalent radius of the cluster, then $P(N)$ can be defined as: $P(N) = \frac{dA(N)}{dr_{equiv}} = \frac{d}{dr_{equiv}}(\pi r_{equiv}^2) = 2\pi\sqrt{N}a$.

The critical nucleus, corresponding to $\eta = \eta_{nucl}$, is defined by $N = N_{crit}$, such that $\frac{d\Delta G(N)}{dN}|_{N_{crit}} = 0$ whence:

$$N_{crit} = \left(\frac{\pi E_{step}a}{ze\eta_{nucl}}\right)^2. \tag{12}$$

3.5.4 Density of nuclei The density of nuclei can be estimated through a stationary balance over adatoms, referred to a representative terrace, conceptually depicted in Fig.10. If the flux term is accounted for in terms of Fick's law for 1D diffusion on a terrace and the space derivative is linearised, setting zero the concentration of adatoms outside of the effective length of the terrace δ, we can write:

$$\frac{zFD}{\delta}C_{ad} = i, \tag{13}$$

where i is the source term due to current density and D is 1D the diffusion coefficient. By solving Eq. (13) with respect to C_{ad} and by using Eq. (7) to

express the current density i with $C = C_0$ (i.e. assuming that mass transport in the electrolyte is highly efficient),

$$C_{ad} = \frac{i_0 \exp\left(-\eta/B_c\right)}{\frac{zFD}{\delta} + \frac{i_0}{C_{ad,o}} \exp\left(\eta/B_a\right)}.$$
(14)

Generalising Eq.(12) to the number N of atoms in a nucleus formed by applying $|\eta| \geq |\eta_{crit}|$, the density of nuclei ρ_n can be defined as $\rho_n\left[\frac{nuclei}{cm^2}\right] = \frac{C_{ad}\left[\frac{mol}{cm^2}\right]}{N\left[\frac{atoms}{nucleus}\right]\frac{1}{N_{Av}}\left[\frac{atoms}{mol}\right]}$ where N_{Av} is Avogadro's number. Hence, by Eq. (14) one obtains:

$$\rho_n = \frac{N_{Av} i_0 \, z \, e \, \eta^2 \, \exp(-\eta/B_c)}{\frac{zFD}{\delta} + \frac{i_0}{C_{ad,o}} \exp(\eta/B_a)}.$$
(15)

It is worth noting that here the definition of η given in Eq. (10) applies. From the micrographs shown in Figs.7-8 one can straightforwardly appreciate the effects of the operating conditions on the density of nuclei.

3.6   Detailed analysis of mass-transport effects

In Section 3.4 mass-transport effects of electroactive species from the electrolyte to the cathode surface have been implicitly accounted for through the surface concentration C. In the present Section we shall provide a more detailed description of the way mass-transport affects electrodic kinetics within a convective diffusion framework.

The starting point of our treatment is Eq.(7). Mass-transport will be accounted for on the basis of the mass-balance for the electroactive species. Under the hypotheses of: (i) steady-state; (ii) diffusive flux; (iii) 1D geometry; (iv) linearisation of the space derivative of concentration in the Fickian diffusive flux, the mass-transport equation reduces to (see also Eq. (13)): $i = \frac{zFD}{\delta}(C_{surf} - C_0)$, where the usual sign conventions apply. In the limiting case of fact ECD reaction, $C_{surf} \to 0$ and the corresponding limiting c.d. is defined by $i_L = -\frac{zFD}{\delta}C_0$, whence:

$$\frac{i}{i_0} = \left(1 - \frac{i}{i_L}\right) \exp\left(-\frac{\eta}{B_c}\right) - \frac{C_{ad}}{C_{ad,o}} \exp\left(\frac{\eta}{B_a}\right),$$

This equation can be usefully restated in the form:

$$i_{tot} = \frac{i_0 \left[\exp\left(-\frac{\eta}{B_c}\right) - \frac{C_{ad}}{C_{ad,o}} \exp\left(\frac{\eta}{B_a}\right)\right]}{1 + \frac{i}{i_0} \exp\left(-\frac{\eta}{B_c}\right)}.$$
(16)
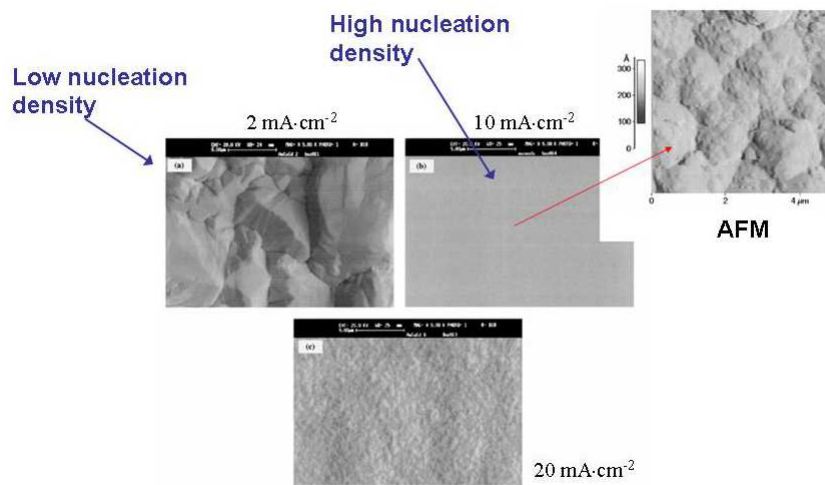
Figure 11. Perturbation of initially flat growth front by step bunching and growth of nuclei. Case of Au-Cu-Cd electrodeposition from a cyanide bath at different current densities. SEM and AFM micrographs, elaborated from [3].

3.7 Destabilisation of an initially planar growth front

As hinted at in the Introduction, ECD growth morphologies are characterised by unstable growth features. The initial stages of such destabilisation can be described in terms of the phenomena described in Sections 3.3 and 3.5. In the presence of additives, the flow of steps can be stopped on some terraces: in this way the steps flowing on terraces above an inhibited one will tend to bunch, forming steps whose height is higher than monoatomic and can reach up to several thousand atomic layers. This is a typical roughening process for systems exhibiting a low nucleation density (Fig.11A, [3]). In cases where the nucleation density is high, roughening correspond to the overgrowth of nuclei (an example of the initial stages of roughening for a system exhibiting a high nucleation density is given in Fig.11B [3]). Such initial stages of roughening can be understood as the perturbation of the initially flat electrodeposit surface, resulting in localisation processes eventually leading to morphogenesis by growth front destabilisation.

The formation of projecting crystallites - ensuing the achievement of full coverage of the cathode surface by the collision of individually growing nuclei - can be rationalised in terms of the simple electrokinetic expressions given in Sections 3.4 and 3.6, emphasizing the inhomogeneity in mass-transport conditions resulting from the formation of outgrowth features, as schematically depicted
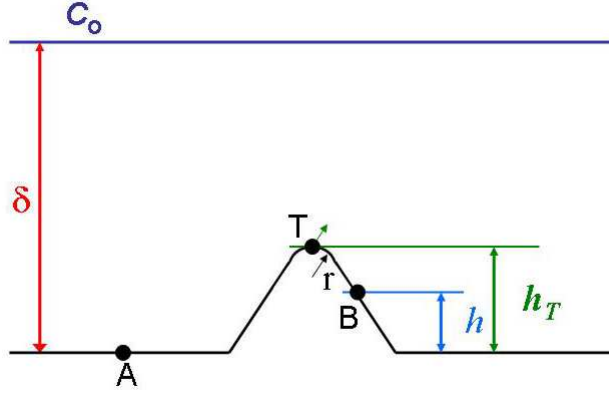
Figure 12. Schematic 1D view of a cathodic outgrowth feature. δ is the concentration boundary layer thickness; h is the coordinate normal to the originally planar cathodic surface, A is a typical position on the flat part of the cathode, B is a typical location on the side of the feature, T represents the tip of the projecting crystallite, r is the radius of curvature of the tip, h_T is the coordinate of the tip.

in Fig.12.

The limiting c.d.s in the typical locations: A (flat part of the cathodes) and B (side of the outgrowth feature) are:

$$i_{L,A} = \frac{zFD}{\delta}C_0 = i_L, \qquad i_{L,B} = \frac{zFD}{\delta - h}C_0 = \frac{\delta}{\delta - h}i_L,$$
$$i_{L,T} = \frac{zFD}{\delta - h_T}C_0 = \frac{\delta}{\delta - h_T}i_L. \tag{17}$$

As far as $i_{L,T}$ is concerned the discussion of point T (tip of the projecting crystallite) requires a distinction between the case in which spherical diffusion conditions develop around the tip or not. The latter case, corresponds to Eq. (17_3). The concentration distribution developing in the electrolyte in this case can be schematised as in Fig.13. Under the simplifying assumption that the thickness of the spherical boundary layer is equal to the radius of curvature r of the tip, a concentration C_{sph} develops at the position of the spherical boundary layer, such that: $C_{sph} = C_0 \dfrac{h_T + r}{\delta}$ whence:

$$i_{L,T} = \frac{zFD}{r}C_{sph} = zFD\frac{h_T + r}{r\delta}C_0 = i_L(1 + \frac{h_T}{r}) \tag{18}$$
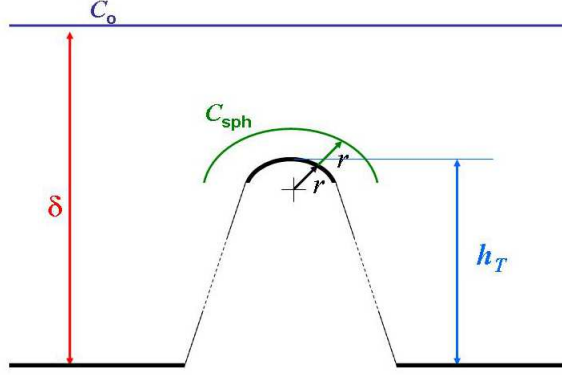
Figure 13. Schematic 1D view of the spherical diffusion boundary layer forming at a cathodic outgrowth feature. δ is the planar concentration boundary layer thickness, r is the radius of curvature of the tip, h_T is the coordinate of the tip, C_0 is the bulk concentration of the electroactive species and C_{sph} that developing at the spherical boundary layer.

Combining Eq.s (16) and (17), one obtains:

$$i_{flat} \equiv i_{Eq.16}, \quad i_{side}(h) = \frac{i_0 \left[\exp\left(-\frac{\eta}{B_c}\right) - \frac{C_{ad}}{C_{ad,o}} \exp\left(\left(\frac{\eta}{B_a}\right)\right) \right]}{1 + \frac{i}{i_0} \frac{\delta}{\delta - h} \exp\left(-\frac{\eta}{B_c}\right)},$$

$$i_{tip}(h_T) = i_{side}(h_T). \tag{19}$$

where $0 \leq h \leq \delta$. Eq. (19) holds in the case where a spherical boundary layer does not develop, otherwise, in the case where a spherical boundary layer develops:

$$i_{tip}(h_T, r) = \frac{i_0 \left[\exp\left(-\frac{\eta}{B_c}\right) - \frac{C_{ad}}{C_{ad,o}} \exp\left(\frac{\eta}{B_a}\right) \right]}{1 + \frac{i}{i_0} \frac{r}{r + h_T} \exp\left(-\frac{\eta}{B_c}\right)}. \tag{20}$$

Under typical cathodic conditions, the following approximation holds:

$$i_0 \left[\exp\left(-\frac{\eta}{B_c}\right) - \frac{C_{ad}}{C_{ad,o}} \exp\left(\frac{\eta}{B_a}\right) \right] \simeq i_0 \exp\left(-\frac{\eta}{B_c}\right). \tag{21}$$

We can thus define the rate equation for charge transfer as

$$i_{ct}(h_T, r) = i_0 \exp\left(-\frac{\eta}{B_c}\right) \tag{22}$$
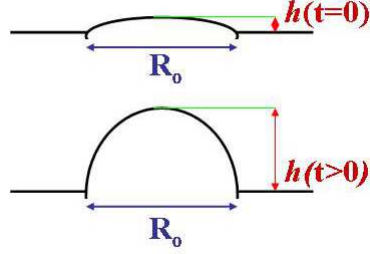
Figure 14. Growth mode of an ellipsoidal hump.
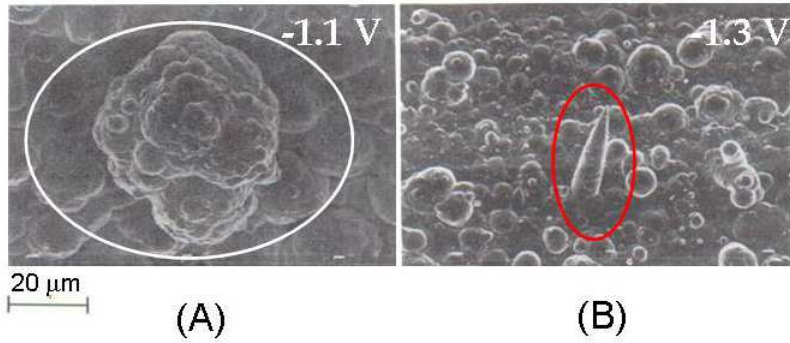
Figure 15. Typical SEM micrographs of outgrowth features. Au-Ag electrodeposits obtained at the indicated potentials from free-cyanide solutions [6].

In view of Eq.s (21) and (22), the following, physically informative approximations are possible for Eq.s(19)-(20), in terms of the ratio $\frac{i_{ct}}{i_L}$:

$$i_{flat} \simeq \frac{i_{ct}}{1 + \frac{i_{ct}}{i_L}}, \quad i_{side}(h) \simeq \frac{i_{ct}}{1 + \frac{i_{ct}}{i_L}\frac{\delta-h}{\delta}}, \quad i_{tip}(h_T, r) \simeq \frac{i_{ct}}{1 + \frac{i_{ct}}{i_L}\frac{r}{r+h_T}} \qquad (23)$$

3.7.1 Rate of growth of a projecting crystallite The growth rate of the side and of the tip of a projecting crystallite can be modelled in terms of Eq.s Eq.s(19)-(20) or (23). In the case of the side, one can write:

$$\frac{dh}{dt} = \frac{V}{zF}(i_{side} - i_{flat}), \qquad (24)$$
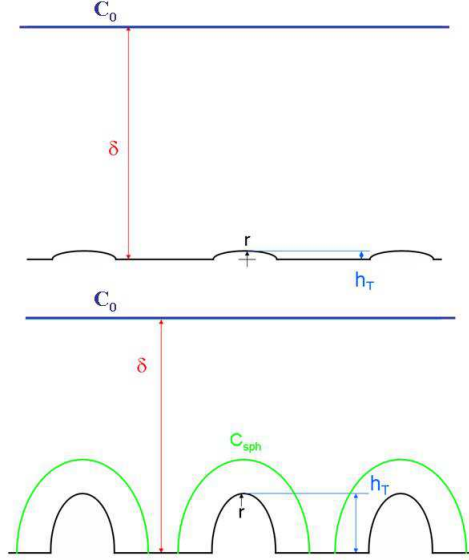
Figure 16. Growth of an array of ellipsoidal humps. Initial stages: planar diffusion conditions prevail, progressed stages: spherical diffusion conditions develop.

where V is the molar volume of the electrodeposited metal. If the polarisation is strongly cathodic and $h \ll \delta$, Eq. (24) simplifies to:

$$\frac{dh}{dt} = \frac{V}{zF} \frac{i_{flat}^2}{i_L} \frac{h}{\delta}. \tag{25}$$

Analogously, in the case of the tip:

$$\frac{dh_T}{dt} = \frac{V}{zF}(i_{tip} - i_{flat}), \tag{26}$$

that, in the case of strong cathodic polarisation and $r \ll h_T$, yields

$$\frac{dh_T}{dt} = \frac{V}{zF} i_{flat} \frac{h_T}{r}. \tag{27}$$

From Eq.s (24-27) it can be concluded that humps forming on the cathode by repeated nucleation or step bunching will tend to be amplified, giving rise to a transition of a given cathodic location from a growth rate typical of "flat" conditions to the "tip" mode. Referring to Fig.14, we assume that an ellipsoidal hump forms on the cathode and that it grows according to the laws described above in this paragraph, keeping the axis Ro constant, e.g. owing to nucleation exclusion (see Section 3.5.2). The growth rate of the tip can be described by
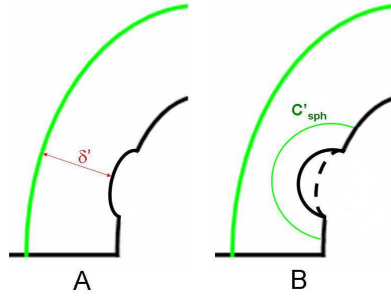
Figure 17. Formation (A) and growth (B) of a second-generation ellipsoidal hump onto a first-generation hump, inside the spherical diffusion layer of the first-generation hump, with formation of a second-generation spherical diffusion layer (light, green line in B), within the first-generation spherical diffusion layer (thick green lines in A and B).

Eq. (23.3). The radius of curvature at the tip is: $r = \frac{R_0^2}{h}$. Since $r(t \simeq 0) \gg 1$, the following approximation holds for the growth rate of the tip:

$$\frac{i_{ct}}{1 + \frac{i_{ct}}{i_L}\frac{r}{r+h_T}} \simeq \frac{i_{ct}}{1 + \frac{i_{ct}}{i_L}} \Rightarrow \quad i_{tip}(h_T, r) \simeq i_{flat} \tag{28}$$

At later times $t > 0$, $r(t) < r(t \simeq 0)$ and the growth at the tip has to be described by Eq. (23.3) without approximations.
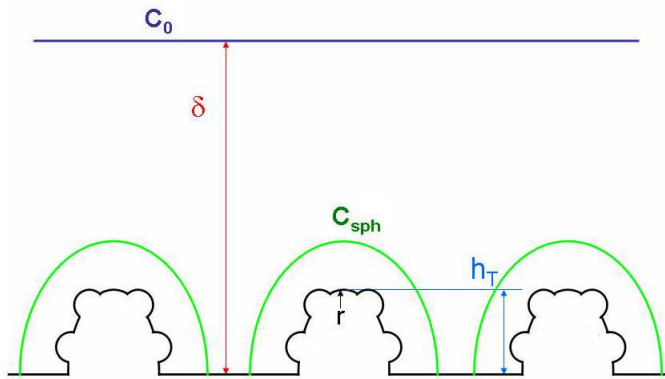
Figure 18. An array of initially spheroidal humps (see Figure A6) develops cauliflower morphology.
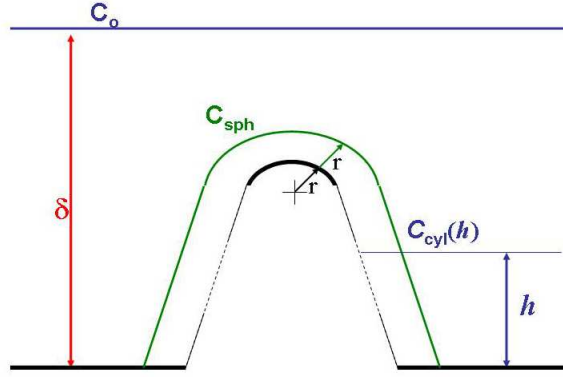
Figure 19. Schematic 1D view of the cylindrical spherical diffusion boundary layer forming at the side of a carrot-like cathodic outgrowth feature. δ is the planar concentration boundary layer thickness, r is the radius of curvature of the tip, h is the coordinate of a given position along the feature stalk, C_0 is the bulk concentration of the electroactive species, C_{sph} that developing at the spherical boundary layer and C_{cyl} the corresponding one for the cylindrical boundary layer.

3.7.2 Cauliflower morphologies It is often experimentally found that ECD humps tend to evolve into cauliflower morphologies. A typical example is given in Fig.15A [6]. Such morphology can be rationalised - as detailed below - as an evolution of the initially ellipsoidal hump discussed in Section 3.7.1. At the initial stages of the growth of an ellipsoidal hump of the type described by Eq. (28) a linear diffusion layer forms, but as growth proceeds (Eq. (23.3)), a spherical diffusion layer is liable to form, provided the hump we are concentrating on is sufficiently far from other ones (see Fig.16). For the same reasons leading to the formation of a hump on a flat cathode, second-generation humps can form onto first-generation ones and, if a first-generation spherical diffusion layer has formed (Fig.17, panel A) the growth of second-generation humps is controlled by its thickness. At later stages, second-generation humps can develop their own (second-generation) spherical diffusion layers (Fig.18). Eq.s (28) and (23.3) - discussed in Section 3.7.1 for an ellipsoidal hump on a flat cathode (first-generation hump), also apply to higher-generation humps. If higher-order spherical diffusion layers form, the growth rate is the same in all directions with respect to the initial flat surface.

3.7.3 Carrot-like and dendritic morphologies If, during the growth of a projecting feature, the condition $\frac{r}{h} \ll 1$ develops (see Fig.13, for the geometri-

cal symbols), then it becomes possible that ECD goes on under charge-transfer control at the tip on under diffusion control at the flat portion of the electrode. Referring to Eq.s (23.1) and (23.3), if $i_{L,flat} \gg i_{ct}$, then

$$i_{flat} \simeq i_{L,flat}, \text{ while } i_{tip}(h_t, r) \simeq i_{ct}, \tag{29}$$

regardless of the value of i_L at the tip. In these conditions, growth of an isolated feature takes place yielding so-called carrot-like features (see Fig.15B). Since process is kinetically characterized by the fact that the growth rate of the tip is constant: (29) into (27) one obtains:

$$\frac{dh_T}{dt} = \frac{V}{zF}(i_{ct} - i_{L,flat}). \tag{30}$$

It is worth noting that in Eq.(30) the tip growth rate exhibits an exponential dependence upon overvoltage η (through the Tafel equation).

Of course, the conditions represented by Eq.s (29) are limiting ones and mixed kinetic control might occur at the tip. On the basis of Eq. (18), one can define a spherical limiting c.d. for the tip, such that (see Fig.13 for the geometrical definitions):

$$i_{L,tip}(h_T, r) = zFD\frac{C_{sph}}{r} \simeq zFDC_0\frac{h_T + r}{\delta}\frac{1}{r} = i_{L,flat}(1 + \frac{h_T}{r}), \tag{31}$$

One can thus write the c.d. at the tip in the form:

$$i_{tip}(h_T, r) \simeq \frac{i_{ct}}{1 + \frac{i_{ct}}{zFDC_0}\delta\left(\frac{r}{r+h_T}\right)^2} \simeq \frac{i_{ct}}{1 + \frac{i_{ct}}{i_{L,flat}}\left(\frac{r}{h_T}\right)^2}$$

yielding the growth law $\frac{dh_T}{dt} = \frac{V\,i_{L,flat}}{zF}\frac{(\alpha-1)h_T^2 - \alpha\,r^2}{h_T^2 + \alpha\,r^2}$, where: $\alpha = i_{ct}/i_{L,flat}$, that after integration, yields: $t = (\alpha-1)h_T - r\alpha\sqrt{\alpha}\,tg^{-1}\left(\frac{h_T}{r\sqrt{\alpha}}\right)$ exhibiting clear limiting cases for $\frac{r}{h_T} \ll 1$ and $\alpha \gg 1$.

3.7.3a Branching   In the above-sketched treatment we have considered that at the tip growth goes on by charge-transfer or mixed control at the tip - under spherical diffusion -, while at the flat portion of the electrode, growth occurs at the limiting c.d. defined by planar diffusion: these conditions ensure carrot-like growth. Nevertheless, in analogy with what has been described to occur in the case of cauliflower morphology formation: (i) humps can form on the sides of carrots and (ii) cylindrical diffusion conditions can set in at the sides of a carrot-like feature (Fig.19). For the present discussion it is useful to
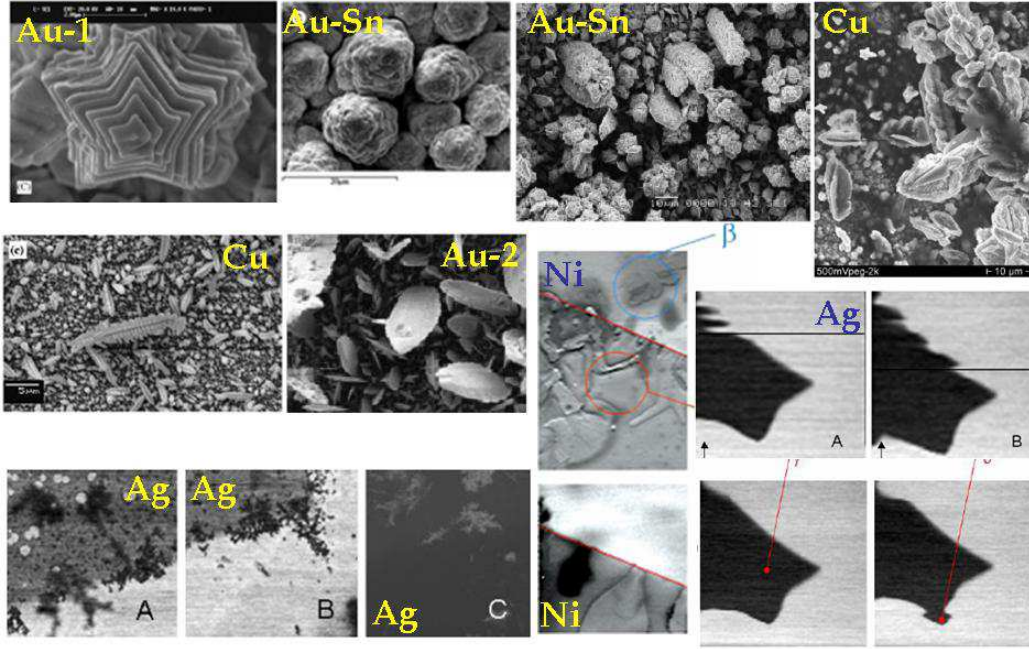
Figure 20. A selection of dendritic morphologies, grown by electrodeposition of the indicated metals and alloys: Au-1 [4], Au-Sn [7], Cu [8], Au-2 [16], Ni [17], Ag [13].

derive an expression for the limiting c.d. under cylindrical diffusion, in analogy with Eq.s (17) and (31) for the planar and spherical diffusion cases, that is

$$i_{L,side}(h,r) = zFD\frac{C_{cyl}}{r} \simeq zFDC_0\frac{h}{\delta}\frac{1}{r} = i_{L,flat}\frac{h}{r}. \qquad (32)$$

Humps developing on the sides of carrot-like features can thus grow inside the cylindrical diffusion layer like in the case of cauliflower morphologies: according to the $i_{ct}/i_{L,side}$ ratio, such features can keep a globular morphology (growth of second-order features under spherical diffusion mass-transport control) (Fig.20, top left micrograph) or outgrow into secondary carrot-like crystallites, giving rise to branched dendrites (growth of second-order features under charge-transfer control) (Fig.20). This typically occurs when separated secondary nuclei form, that can subsequently grow independently (for relevant details, see Section 3.5.4).
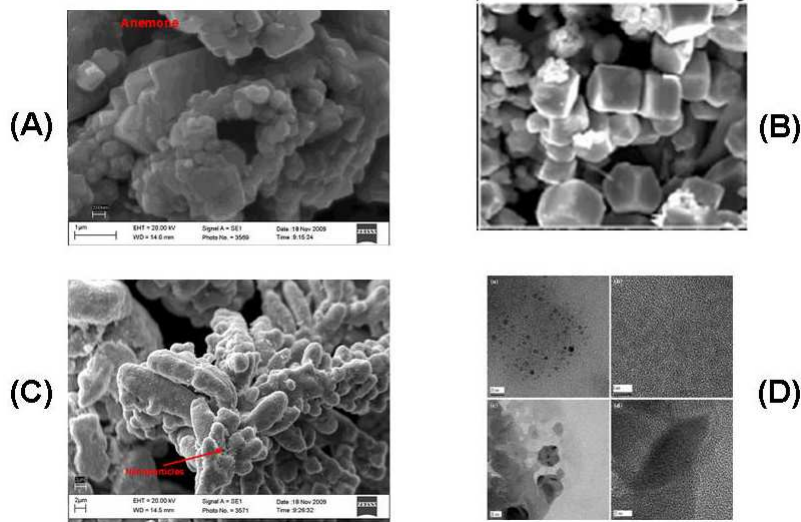
Figure 21. A selection of classical morphologies for powdered Cu electrodeposits. (A) Nano-anemones SEM [23]; (B) nano-dices SEM [12]; (C) nano-particles supported on dendrites SEM [23]; (D) Freestanding nano-particles HRTEM [11].

3.7.3b Powdered deposits - In an introductory theory, powdered deposits can be considered to derive from dendritic growth followed by mechanical rupture of the outgrowth features, as a result of fluid motion or gravitational effects. Some examples are shown in Fig.21. In a more advanced treatment, bipolar [23] and combined chemical-electrochemical [11, 12] effects ought to be considered.

3.7.3c Filamentary and spongy deposits - These types of morphologies - a selection of examples in proposed in Fig.22 - can be regarded as the development of carrot-like growth types developing from higher-generation humps in cauliflower-type deposits.

3.8   Levelling effects

The destabilizing effects discussed in Section 3.7 tend to be obnoxious towards industrial ECD and counteractions are needed in order to avoid them. A typical approach is the use of leveling additives. In Fig.23 we report some experimental results obtained in our laboratory. The real action of these substances is complex and generally poorly know, but can be simply modelled as proposed in this Section. Of course, the critical situation for metal plating without ir-
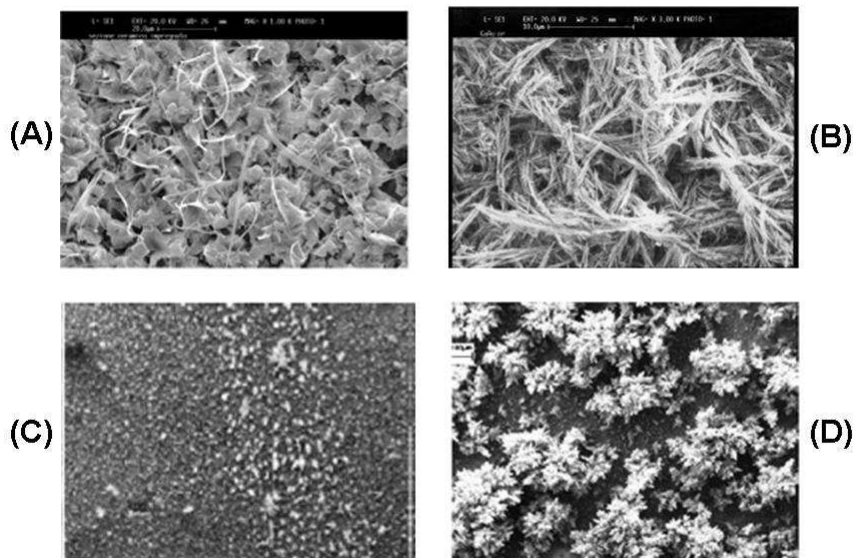
Figure 22. A selection of filamentary and spongy morphologies. (A) Cu/MgO composite [5]; (B) Zn-Te [2]; (C) Au electrodeposited onto an electrode functionalised with a thiol SAM [20]; (D) Au electrodeposited from a liposome-based bath [20].

regularities is when ECD goes on at the limiting current density. As detailed in Section 3.7, the localisation of different growth rates in different positions due to local differences in mass-transport or to the fact that in some position deposition goes on under charge-transfer limited conditions, while in some other regions, growth occurs under mass-transport control, leads to the amplification of irregularities. From this point of view, the aim of additives can be regarded as that of inhibiting growth on tips and to enhance it in recesses. A simple, but physically sound modelling assumption - derived from [27] pp. 63s - is that the additive reacts cathodically and its reaction rate is mass-transport limited on all cathode features. According to this assumption, the following electrochemical reaction mechanism can be conjectured for the additive:

$$\text{Additive} + z^* e^- \rightarrow \text{Product.}$$

Hereinafter the star denotes quantities referring to the additive. Furthermore:

$$i^*_{L,flat} = \frac{z^* F D^*}{\delta} C_0^*, \qquad i^*_{L,tip} = \frac{z^* F D^*}{\delta - h_T} C_0^*. \tag{33}$$
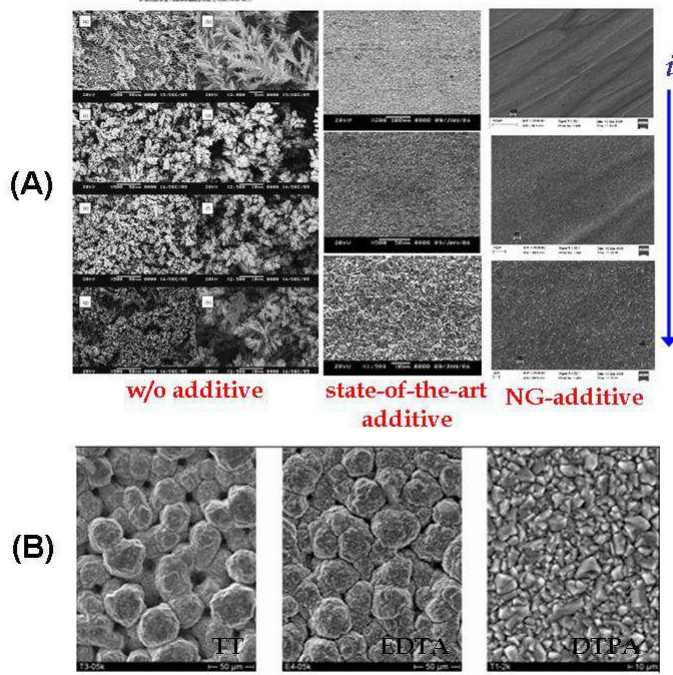
Figure 23. Smoothing effects obtained by using additive systems. (A) Cu: without additive, with state-of-the-art additive, with next-generation additive; current density i increases as indicated by the blue arrow [9]; (B) Mn with the indicated additives, yielding progressively come compact morphology [18].

Of course, in the absence of additives (denoted by w/o for *without*), according to Eq. (17) the metal growth c.d. is:

$$i^{w/o}_{metal,flat} = \frac{zFD}{\delta}C_0, \qquad i^{w/o}_{metal,tip} = \frac{zFD}{\delta - h_T}C_0. \tag{34}$$

Since the additive works as an inhibitor or for the ECD process, of course the metal growth c.d.:

$$i^{wa}_{metal,flat} = i^{w/o}_{metal}\left(1 - \frac{i^*}{i^*_a}\right) \tag{35}$$

where i^*_a indicates the reaction rate of the additive when it is reacting cathodically in the absence of metal plating, i.e. it is an intrinsic molecular property of the additive. In this sense, the quantity $\frac{i^*}{i^*_a}$ represents the cathodic current efficiency of the additive when it reacts during metal plating: since metal plating also brings about the development of outgrowth features, of course i^* also
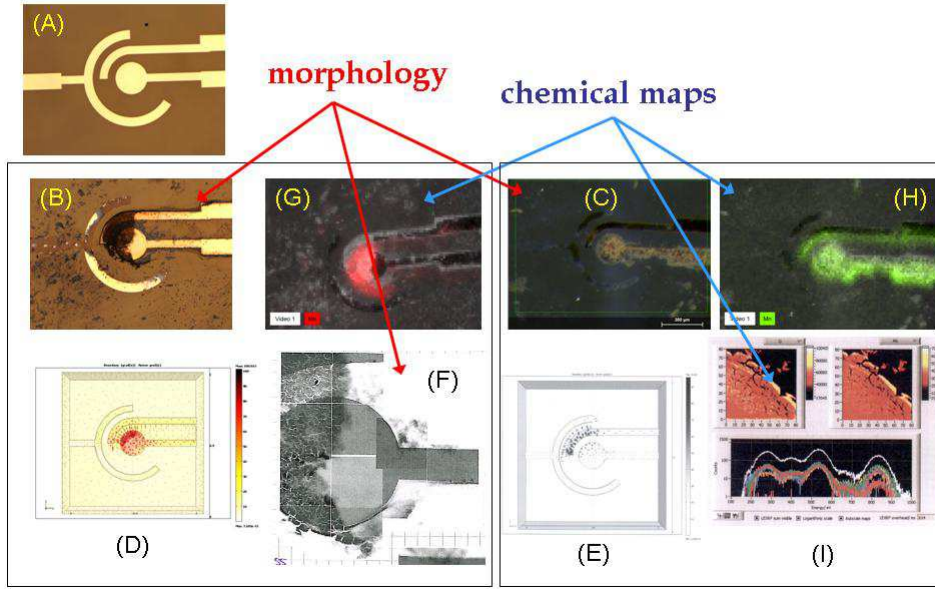
Figure 24. Coupling of morphology and surface composition in Au-Mn electrodeposition: imaging by optical microscopy (A-C) and Soft X-ray Transmission Microscopy (F); space-resolved compositional analysis by conventional (G, H) and syncrotron-based (I) X-ray fluorescence spectroscopy; panels (D, E) report numerical computations of the growth rate distribution.

takes this contribution into account. Rewriting Eq. (35) for the flat part of the cathode and for the tip, and using Eq.s (33)-(34), the following equations result:

$$
\begin{aligned}
i_{metal,flat}^{wa} &= \frac{zFDC_0}{\delta}\left(1 - \frac{z^*FD^*C_0^*}{\delta i_a^*}\right), \\
i_{metal,tip}^{wa} &= \frac{zFDC_0}{\delta - h_T}\left(1 - \frac{z^*FD^*C_0^*}{(\delta - h_T)i_a^*}\right).
\end{aligned}
\tag{36}
$$

whence it follows that $i_{metal,flat}^{wa} = i_{metal,tip}^{wa}$ for

$$
\frac{z^*FD^*C_0^*}{i_a^*} = \frac{\delta(\delta - h_T)}{2\delta - h_T}.
\tag{37}
$$

Since, at the initial stages of ECD unstable features are still small and $\delta \gg h_T$, one can approximate the RHS of Eq. (37) with $\delta/2$, yielding a guideline
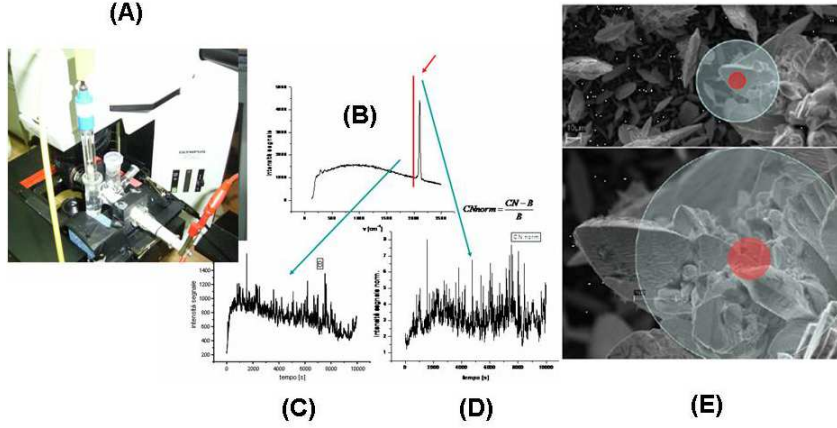
Figure 25. Coupling of morphology and surface composition in Au electrodeposition from cyanocomplexes: (A) photograph of the electrochemical cell mounted on the Raman spectromicroscope; (B) Surface-enhanced Raman spectrum of adsorbed cyanide; (C) time series of the cyanide peak intensity, (D) time series of the background intensity, (E) SEM micrographs of electrodeposited Au. The blue and red disks indicate the areas sampled by space-resolved Raman spectroscopy. For details, see [16].

for the choice of the additive system in terms of its molecular properties (i_a^*), concentration (C_0^*) and fluid-dynamics of the ECD bath (δ). Of course, by tuning around the equality set by Eq. (37) it is possible to enhance the growth on the flat regions with respect to the tips and vice versa.

It is worth reporting here that [27] pp. 63s adds a second, much stronger assumption, that notably simplifies the mathematics: in the presence of the additive the total cathodic current density (i.e. the sum of the partial current densities for metal electrodeposition and additive reduction) is constant at all positions of the cathode, i.e., with the symbols defined above,

$$i_{tot} = i_{metal}^{wa} + i^* = i_{metal,flat}^{wa} + i_{flat}^* = i_{metal,tip}^{wa} + i_{tip}^*.$$

whence it follows that

$$i_{metal,flat}^{wa} = i_{tot} - \frac{z^* F D^* C_0^*}{\delta}, \qquad i_{metal,tip}^{wa} = i_{tot} - \frac{z^* F D^* C_0^*}{\delta - h_T}. \qquad (38)$$

Eq.s (38) correspond to an enhancement of the growth rate at the flat parts of the electrodes and an inhibition at the tips.
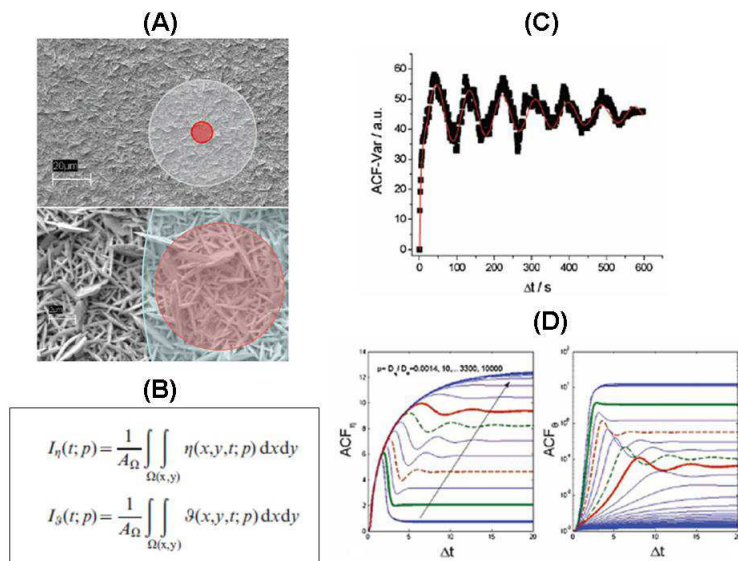
Figure 26. A selection of results from [16], highlighting the simulation of temporal autocorrelation functions (ACF) with the model of Eq.(39) in the case of Au electrodeposition from cyanocomplexes. (A) scanning electron micrograph of Au morphology (for details, see text). (B) η and θ obtained from Eq.(39) are integrated spatially in order to match the space resolution of the microscope and of the spectrometer. (C) A typical measured temporal ACF of the surface concentration of cyanide. (D) Computed ACFs for η and θ.

4 Review of reaction-diffusion modelling of morphogenesis in electrodeposition

As hinted at in the Introduction, we have recently proposed a mathematical model for the description and prediction of morphogenesis in electrodeposition, based on a reaction-diffusion approach [16, 18, 19, 23, 24]. In particular, we developed a system of two reaction-diffusion equations one for the morphology - treated as a continuous quantity - and one for the surface concentration of a key adsorbate. So far, we have shown that the peculiarities of the coupling of morphological and surface chemical dynamics allows to gain understanding and control over 3D metal growth processes. In the rest of this section we will review our key results, leaving out the details, that can be recovered from the original papers. The conceptual origin of our reaction-diffusion model lies in the fact that space-resolved in situ spectroscopic studies carried out in the past decade in our laboratory, have revealed a notable synergy between local surface chemistry, local growth rate and morphology. Local surface chemistry is essentially

controlled by the adsorption at the growing cathodic surface of: (i) additives, such as levellers and brighteners; (ii) ligands released from the complexes used as a source of metal; (iii) products of electrodic side reactions. Two straightforward examples of this phenomenon are offered in Fig.s 24-25. Fig. 24 reports results of an Au-Mn alloy growth experiment, monitored in situ by Soft X-ray Transmission Micro-spectroscopy. Panels (A)-(C) show optical micrographs of the electrode system used for this study in the pristine state (A) and after alloy electrodeposition at two different rates (B) and (C). Panels (D) and (E) show the computed current density distribution for the experiments giving rise to deposits (B) and (C), respectively, computed as illustrated in [21]. (F) is a high-resolution blow-up of (B) obtained by Soft X-ray Transmission Microspectroscopy, yielding detailed information on local thickness. Space-dependent chemical information for the two kinds of deposits was obtained by X-ray Fluorescence mapping with lateral resolutions of ca. 10 mm (G), (H) and ca. 0.1 mm (I), obtained with a conventional X-ray tube (G-, H) and with a synchrotron light source (I). Fig.25 highlights the correlation obtained by Raman spectro-microscopy. Panel (A) shows the electrochemical section of the experimental setup; panel (B) shows a typical spectrum, with a peak corresponding to adsorbed cyanide and a background related to roughness); panel (C) space- and time-resolved Surface Enhanced Raman Spectroscopy of adsorbed cyanide; (D) space- and time-resolved spectral Raman background and panel (E) shows morphology of Au growth as revealed by SEM [16]. Based on this and related evidence, we have tried to develop a modelling framework to treat these phenomena.

For the electrokinetic reasons detailed in [19, 22], we have written the following system of reaction-diffusion equations for the electrode morphology $\eta(x, y, t)$ and the surface coverage with the controlling adsorbate $\theta(x, y, t)$ on a representative domain $\Omega = \Omega_x \times \Omega_y \subset R^2$ and $t \in [0, t_f]$:

$$
\begin{cases}
\dfrac{\partial \eta}{\partial t} = D_\eta \nabla^2 \eta + A \dfrac{\eta^2}{1+\eta} - B\eta\theta, \\
\dfrac{\partial \theta}{\partial t} = D_\theta \nabla^2 \theta + C(1-\theta)\exp(a\,\eta + b\,\theta) - D\theta\exp(c\,\eta + d\,\theta), \\
n \cdot \nabla\eta = n \cdot \nabla\theta = 0, \ \forall(x, y) \in \partial\Omega, t > 0, \\
\eta(x, y, 0) = \eta_0(x, y), \theta(x, y, 0) = \theta_0(x, y), \quad (x, y) \in \Omega.
\end{cases}
\tag{39}
$$

where: A, B, C, D, a, b, c and d are positive real constants. The source terms contain the following contributions:

(i) $\dfrac{\eta^2}{1+\eta}$ expresses non-linear charge-transfer electrokinetics;

(ii) $\eta\theta$ accounts for the inhibition of the ECD process by adsorbates;
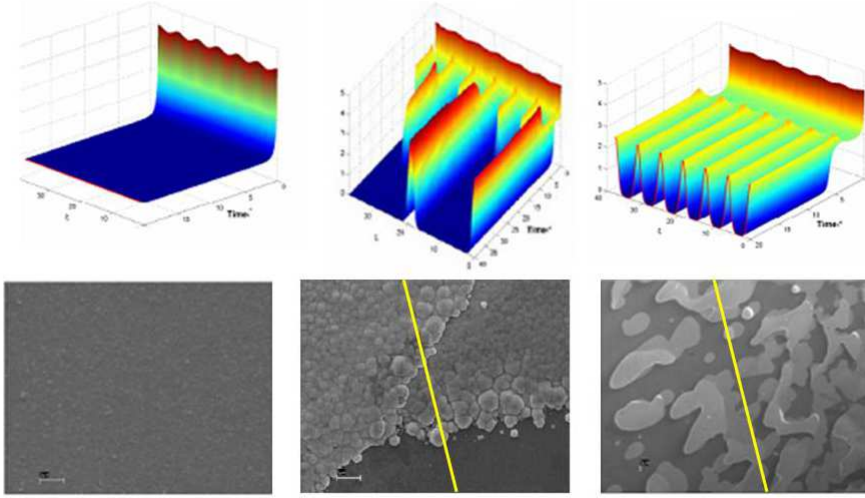
Figure 27. A selection of data from [10, 14], showing the results of 1D numerical solutions of Eq.(39) of , obtained with parameters corresponding to changes in the growth chemistry of Au-Cu alloys: the corresponding SEM micrographs are reported below the plots. Owing to the compositional contrast of this particular alloy, the micrographs convey simultaneously information on morphology and chemical distribution.

(iii) $(1 - \theta) \exp(a\,\eta + b\,\theta)$ and $\theta \exp(c\,\eta + d\,\theta)$ and account for electrochemically controlled adsorption and desorption, respectively: such terms also contain contribution for the lateral interaction of adsorbates.

4.1   Simulation of 2D morphological and chemical dynamics

In a first set of experiments ([16], for experimental details, see Fig.25 and corresponding comments), we have validated this approach by comparing the autocorrelation functions (ACF) of measured and computed time series of morphological and chemical quantities. A selection of results is shown in Fig.26. In order to match the space resolution of a scanning electron micrograph (SEM, Panel (A)) and of the Raman spectrometer (blue and red circles superimposed on the SEM images), we have integrated the results of the numerically solved quantities η and θ (see Eq. (39)) over the analysis spot (panel (B)). Panel (C) shows a typical measured temporal ACF of the surface concentration θ of cyanide, while panel (D) reports computed ACFs for η and θ, for several sets of parameters. Our results have shown that sound qualitative matching is found between experimental ACFs and their numerical estimates obtained with Eq. (39).
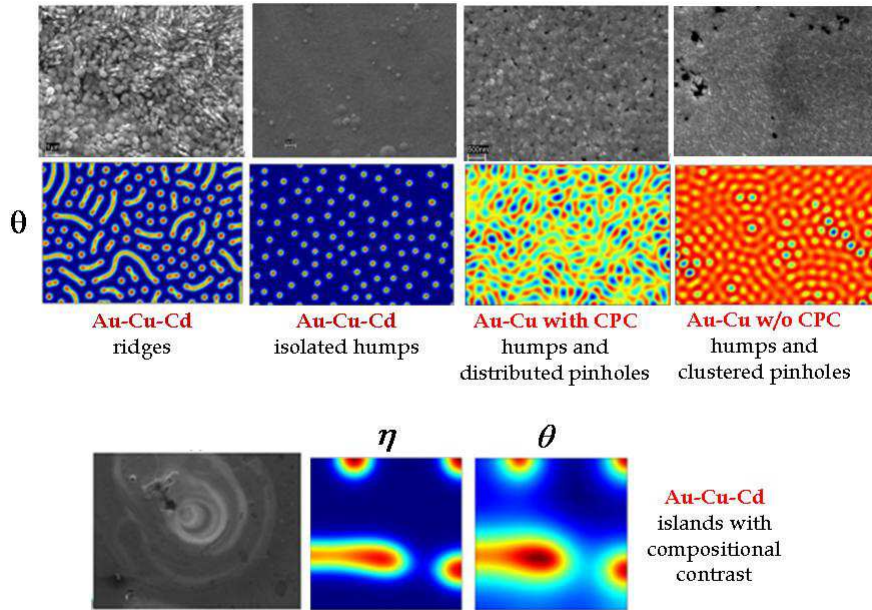
Figure 28. A selection of data from [19], showing the results of 2D numerical solutions of Eq.(39) of , obtained with parameters corresponding to changes in the growth electrochemistry of Au-Cu (without and with CPC as an additive) and Au-Cu-Cd alloys: the corresponding SEM micrographs are next to the plots. Owing to the compositional contrast of this particular alloy, the micrographs convey simultaneously information on morphology and chemical distribution.

4.2 Turing instabilities

The model expressed by Eq. (39) has been proved to exhibit Turing instabilities in 1D [10, 14] and 2D [18, 19]. Turing or diffusion-driven instability is one of the possible dynamic scenarios of a reaction-diffusion system and corresponds to the case in which a homogeneous steady state is stable to small perturbations in the absence of diffusion, but it becomes unstable to small spatial perturbations when diffusion is present. In turn, Turing instabilities can give rise to pattern formation. In Fig.27 we report a selection of 1D computational results, together with their experimental validation, of the occurrence of Turing instability and development of undulations. The structure predicted by the model corresponds to the distribution of morphological and chemical features found in 1D section of Au-Cu alloys grown from additive-free solutions exhibiting systematic changes
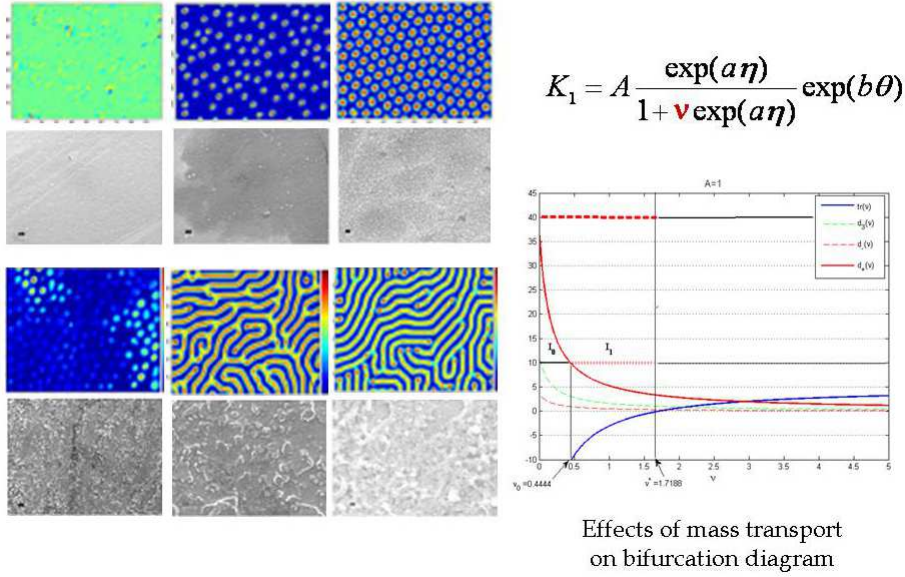
Figure 29. A selection of data from [18], showing the results of 2D numerical solutions of Eq.s (39),(40), including mass-transport effects, gauged by the parameter ν. Experimental results - depicted next to the corresponding graphs of θ - correspond to Mn electrodeposits obtained from a bath based on a room-temperature ionic liquid.

of chemistry, corresponding to parameter variations in the numerical solution of Eq.(39) [10, 14].

Similar, but more detailed results were obtained by solving the 2D version of Eq.(39): a range of patterns were found, that closely match experimental ones found in the electrodeposition of Au-Cu-Cd alloys and Au-Cu solutions, containing CPC as an additive (for details, see [19]): a gallery of morphologies is shown in Fig.28, featuring ridges, isolated humps, isolated and clustered pinholes as well as islands with peculiar compositional distributions.

In [18] we have introduced mass-transport effects in the electrokinetics of the equation for θ in (39), resulting in

$$\frac{\partial \theta}{\partial t} = D_\theta \nabla^2 \theta + C(1 - \theta)\frac{\exp(a\,\eta + b\,\theta)}{1 - \nu \exp(a\,\eta)} - D\theta \exp(c\,\eta + d\,\theta), \qquad (40)$$

where the coefficient ν is the reciprocal of the limiting current density. As expected, the Turing patterns are affected by the entity of the mass-transport contribution, as highlighted in Fig.29, reporting numerical and experimental results regarding the electrodeposition of Mn from a room-temperature ionic liquid.
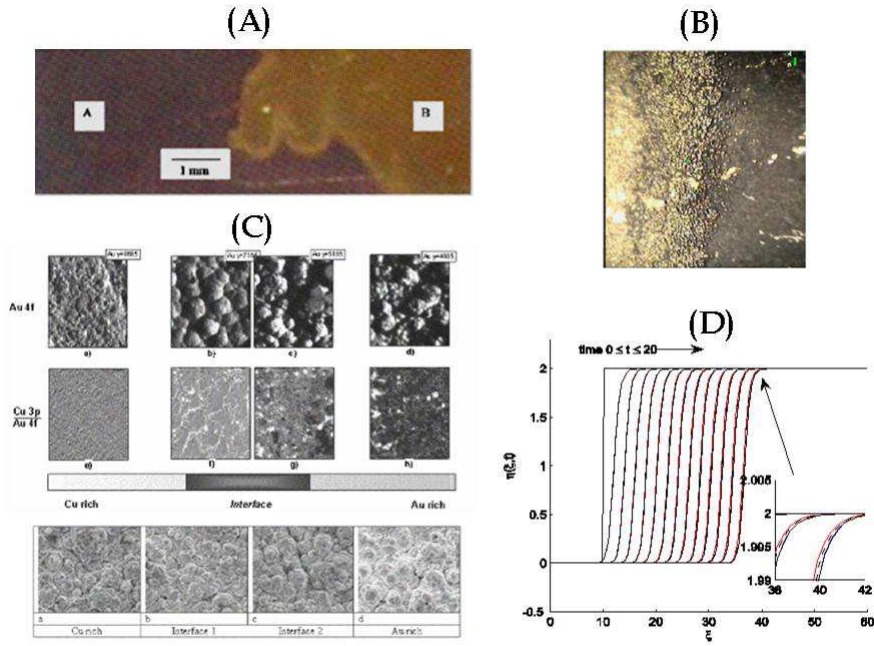
Figure 30. A selection of data from [15], showing snapshots of coupled compositional/morphological travelling waves obtained during electrodeposition of Au-Cu from a free-cyanide solutions. (A) Macrograph; (B) optical micrograph, (C) scanning photoelectron micrographs, measured at the Au energy; (D) the results of the numerical simulation of with Eq. (39).

4.3   Travelling waves

With a suitable choice of parameters, Eq. (39) has also been shown to support solutions of the travelling-wave type [15, 22]. Travelling waves are indeed found in specific instances of electrodeposition and give rise to particularly evident effects - that can sometimes be perceived with the naked eye - when coloured alloys are electrodeposited: this is the case of Au-Cu obtained from free-cyanide solutions: a selection of micrographs - obtained with imaging techniques indicated in the figure caption - and the results of numerical simulations are shown in Fig.30.
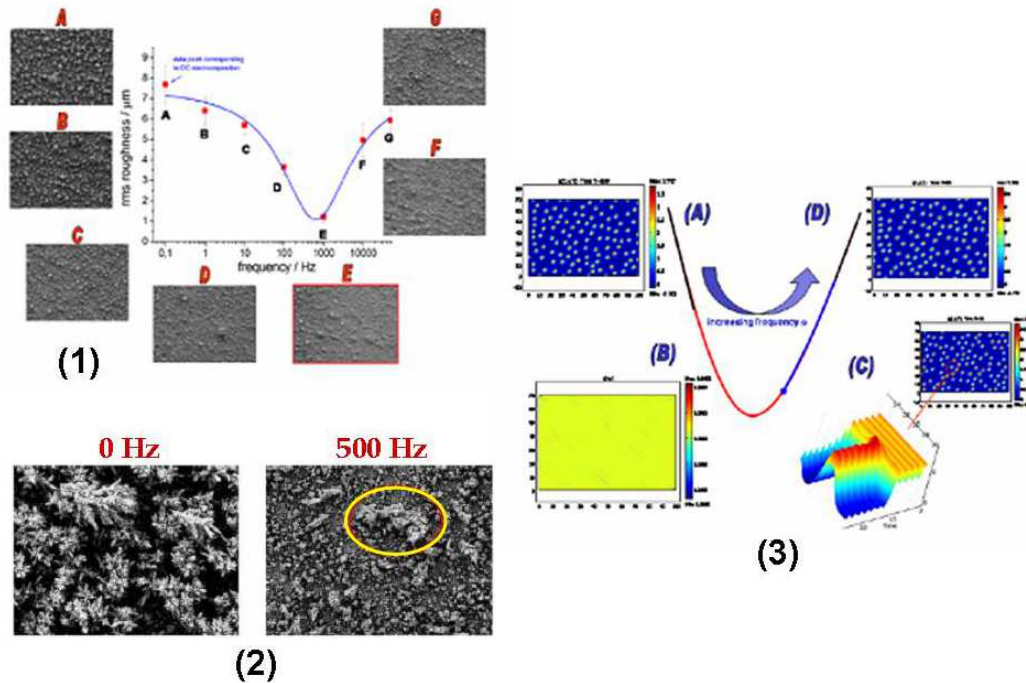
Figure 31. A selection of data from [24], showing the effects of a small-amplitude forcing term on the morphology of electrodeposited Au. (1) Electrodeposit roughness as function of frequency: SEM micrographs and measured roughness. (2) Comparison of the effects of the indicated frequencies: higher magnification SEM. (3) Numerical simulations of the asymptotic morphologies (Eq.(39) with a added sinusoidal forcing term).

4.4 Effects of forcing term

In [24] we have shown that smoothing effects can be achieved in potentiostatic metal electroplating processes if a small-amplitude (ca. 10mV) potential sinusoid - of frequency contained in an appropriate range (a few hundred Hz) - is summed to the applied DC bias. Similar smoothing effects are typically obtained in the industrial practice with the addition of toxic chemicals to the process solutions. By adding a sinusoidal forcing term on the equation for η of Eq. (39) , this results can be explained in terms of the coupling between the dynamics of processes controlling the time evolution of metal morphology and interfacial chemistry. Fig.31 highlights the effect of such periodic external forcing on the Turing patterns found in the unforced case, pinpointing the influence of the periodic driving force in pattern suppression. The observed morphology

of Au electrodeposits matches the computational result in a surprising way. Our results show that an insightful understanding of the dynamics of reacting systems can offer green solutions to problems that are traditionally attacked with the use of non-sustainable chemistries.

5 Conclusions

Electrocrystallisation is an experimental science and the phenomenological morphogenesis is the result of subtle and often poorly understood and controlled processing parameters as well as of their mutual interaction. Nevertheless, morphology types can be regarded as well assessed and their classification is acceptable for both scientific and technological purposes. The current understanding of phenomenological morphogenesis offers a system of sound ex post explanation schemes in terms of relative contributions of processing parameters. This approach has been systematised and unified with the simple models presented in Section 2. Notwithstanding the possibility of rationalising electrochemical metal growth processes, the available approaches exhibits serious limitations in predictive capability. For this reason, more insightful modelling of electrodeposition dynamics is needed, chiefly in view of: (i) active control of growth, in which the actual morphological observable is fed back for the actuation of the processing parameters; (ii) predictive morphology tailoring, mainly for the implementation of bio-inspired crystallisation schemes. A step in this direction is provided by the reaction-diffusion model set up by the authors (reviewed in Section 4), that highlights the synergy between morphology and surface chemistry. This approach has demonstrated a notable degree of predictive power (Sections 4.1-4.3) as well as its adequacy for automatic control applications (Section 4.4). The next challenges for the extension of this approach are: (i) incorporation of mass-transport contributions into the electrokinetic expression; (ii) introduction of mechano-electrochemical coupling and (iii) consideration of stochastic source terms.

References

[1] Peraldo Bicelli L., Bozzini B., Mele C., D'Urzo L.: *A Review of Nanostructural Aspects of Metal Electrodeposition.* Int. J. Electrochem. Sci. **3**, 356-408 (2008).

[2] Bozzini B., Baker M.A., Cavallotti P.L., Cerri E., Lenardi C.: *Electrodeposition of ZnTe for Photovoltaic Cells.* Thin Solid Films, 361-362, 388-395 (2000).

[3] Bozzini B., Cavallotti. P.L.: *Electrodeposition and characterization of Au-Cu-Cd alloys.* J. Appl. Electrochem. **31**, 897-903 (2001).

[4] Bozzini B., Fanigliulo A., Serra M.: *Electrodeposition of star-shaped gold crystallites.* J. Crystal Growth **231**, 589-598 (2001).

[5] Bozzini B.: *Electrochemical pore-filling of ceramics with metal fibers.* J. Mat. Sci. Lett. **20**, 867-868 (2001).

[6] Bozzini B., De Gaudenzi G.P., Mele C.: *A SERS investigation of the electrodeposition of Ag-Au alloys from free-cyanide solutions.* J. Electroanal. Chem. **563**, 133-143 (2004).

[7] Bozzini B., Cavallotti P.L., Fanigliulo A., Giovannelli G., Mele C., Natali S.: *Electrodeposition of white gold alloys: an electrochemical, spectroelectrochemical and structural study of the electrodeposition of Au-Sn alloys in the presence of 4-cyanopyridine.* J. Solid State Electrochem. **8** 147-158 (2004).

[8] Bozzini B., Mele C., D'Urzo L., Giovannelli G., Natali S.: *Electrodeposition of Cu from Acidic Sulphate Solutions in the Presence of PEG: An Electrochemical and Spectroelectrochemical Investigation. Part I.* J. Appl. Electrochem. **36**, 789-800 (2006).

[9] Bozzini B., D'Urzo L., Mele C.: *A novel polymeric leveller for the electrodeposition of copper from acidic sulphate bath: a spectroelectrochemical investigation.* Electrochim. Acta **52**, 4767-4777 (2007).

[10] Bozzini B., Lacitignola D., Sgura I.: *Turing Instability in an Electrodeposition Morphogenesis Model: An Analytical, Numerical and Experimental Study. Computation in Modern Science and Engineering.* Proceedings of the International Conference on Computational Methods in Science and Engineering 2007. T.E. Simos, G. Maroulis Ed.s. American Institute of Physics, CP963, Vol. 2 Part A, 465-468 (2007).

[11] Bozzini B., D'Urzo L., Re M., De Riccardis F.: *Electrodeposition of Cu from acidic sulphate solutions containing cetyltrimethylammonium bromide (CTAB).* J. Appl. Electrochem. **38**, 1561-1569 (2008).

[12] Bozzini B., D'Urzo L., Mele C.: *Electrochemical Fabrication of Nano- and Micrometric Cu Particles: In Situ Investigation By Electroreflectance and Optical Second Harmonic Generation.* Trans. Inst. Met. Fin. **86**, 267-274 (2008).

[13] Bozzini B., D'Urzo L., Gianoncelli A., Kaulich B., Kiskinova M., Prasciolu M., Tadjeddine, A.: *In situ soft X-ray dynamic microscopy of electrochemical processes.* Electrochem. Comm. **10**, 1680-1683 (2008).

[14] Bozzini B., Lacitignola D., Sgura I.: *A Reaction-diffusion model of spatial pattern formation in electrodeposition.* J. of Physics: Conf. Series **96** 012051 (2008).

[15] Bozzini B., D'Urzo L., Gregoratti L., Tadjeddine A: *Study of surface compositional waves in electrodeposited Au-Cu alloys by synchrotron-based high lateral-resolution X-ray photoemission spectroscopy.* J. Electrochem. Soc. 155 (2008) F165-F168.

[16] Bozzini B., D'Urzo L., Lacitignola D., Mele C., Sgura I., Tondo E.: *An investigation into the dynamics of Au electrodeposition based on the analysis of SERS spectral time series.* Trans. Inst. Met. Fin. **87**, 193-200 (2009).

[17] Bozzini B., D'Urzo L., Gianoncelli A., Kaulich B., Prasciolu M., Sgura I., Tondo E., Kiskinova M.: *An in-situ synchrotron-based soft X-ray microscopy investigation of Ni electrodeposition in a thin-layer cell.* J. Phys. Chem. C. **113**, 9783-9787 (2009).

[18] Bozzini B., Sgura I., Lacitignola D., Mele C., Marchitto M., Ciliberto A.: *Prediction of Morphological Properties of Smart-Coatings for Cr Replacement, Based on Mathematical Modelling.* Adv. Mat. Res. **138**, 93-106 (2010).

[19] Bozzini B., Lacitignola D., Sgura I.: *Morphological spatial patterns in a reaction diffusion model for metal growth.* Mathematical Biosciences and Engineering **7**, 237 - 258 (2010).

[20] Bozzini B., D'Urzo L., Mele C., Busson B., Tadjedine A.: *Au electrodepostion in presence of self-assembling organics: in situ study by sum frequency generation and surface enhanced Raman spectroscopy.* Trans. Inst. Met. Fin. **88**, 130-143 (2010).

[21] Bozzini B., Gianoncelli A., Kaulich B., Kiskinova M, Prasciolu M., Sgura I.: *Metallic Plate Corrosion and Uptake of Corrosion Products by Nafion in Polymer Electrolyte Membrane Fuel Cells.* ChemSusChem **7**, 846-850 (2010).

[22] Bozzini B., Lacitignola D., Sgura I.: *Travelling waves in a reaction-diffusion model for electrodeposition.* Mathematics and Computers in Simulation **81**, 1027-1044 (2011).

[23] Bozzini B., Guerrieri M., Capotondi F., Sgura I., Tondo E.: *Electrochemical preparation of particles for X-ray free electron laser based diffractive imaging.* Int. J. Electrochem. Sci. **6**, 2609 - 2631 (2011).

[24] Bozzini B., Lacitignola D., Sgura I.: *Frequency as the greenest additive for metal plating: mathematical and experimental study of forcing voltage effects on electrochemical growth dynamics.* Int. J. Electrochem. Sci. **6**, 4553-4571 (2011).

[25] Giovannelli G., Natali S., Bozzini B.: *Silver coated lead coins: An appraisal of ancient technology.* J. Appl. Electrochem. **36**, 951-956 (2006).

[26] Mele C., Rondinini S., D'Urzo L., Romanello V., Tondo E., Minguzzi A., Vertova A., Bozzini B.: *Silver electrodeposition from water-acetonitrile mixed solvents and mixed electrolytes in the presence of tetrabutylammonium perchlorate. Part I: electrochemical nucleation on glassy carbon electrode.* J. Solid State Electrochem. **13**, 1577-1584 (2009).

[27] Popov K.I., Djokic S.S., Grgur B.N.: Fundamental Aspects of Electrometallurgy. Kluwer Academic / Plenum Publishers, NY (2002) Chapters 2 and 3.

[28] De Riccardis M.F., Carbone D., Martina V., Re M., Bozzini B., D'Urzo L.: *Study on the adhesion mechanism of electrodeposited nickel clusters on carbon substrates.* Applied Surface Science **255**, 4309-4315 (2009).